Nanoscale

PAPER

View Article Online
View Journal

Cite this: DOI: 10.1039/c9nr07777d

A multiple mode integrated biosensor based on higher order Fano metamaterials†

Xin Yan,‡[a] Zhang Zhang,‡[b] Lanju Liang,[a] Maosheng Yang, *[c] Dequan Wei,[a] Xiaoxian Song,[c] Haiting Zhang,[c] Yuying Lu,[b] Longhai Liu,[d] Mengjin Zhang,[e] Tao Wang[e] and Jianquan Yao[b]

Received 10th September 2019,
Accepted 30th November 2019

DOI: 10.1039/c9nr07777d

rsc.li/nanoscale

A multiple mode integrated biosensor based on higher order Fano metamaterials (FRMMs) is proposed. The frequency shifts (Δf) of x-polarized quadrupolar (Q_x), octupolar (O_x), hexadecapolar (H_x), y-polarized quadrupolar (Q_y) and octupolar (O_y) Fano resonance modes are integrated to detect the concentration of lung cancer cells. In experiments, the concentrations of lung cancer cells can be distinguished by the shape and distribution of integrated graphics. In addition, an anomalous response in Δf in resonant mode is surprisingly observed. As the cell concentration increases, the Δf at the Q_x-dip, Q_y-dip and O_y-dip successively experiences an increasing frequency shift stage (IFSS), decreasing frequency shift stage (DFSS) and re-increasing frequency shift stage (RIFSS). The extraordinary DFSS confirmed by single-factor analysis of variance (ANOVA) means an unusual physical phenomenon in metamaterial biosensors. By introducing a new dielectric constant ε_f, we amend perturbation theory to explain the unusual phenomenon in Δf. With the change of the mode order from Q_x to H_x, the ε_f increases from −2.78 to 0.75, which implies that the negative ε_f leads to the appearance of the DFSS. As a platform for biosensing, this study opens a new window from the perspective of multiple mode integration.

Introduction

Biosensing has a profound impact on life science and biological medicine; especially, since living cancer cells are closely related to various physiological processes, the successful detection of these cells turns out to be significant and of great potential in the fields of cytology, bio-medicine and bio-molecules. Commonly, one of the most used methods is the labelling-based fluorescence technique, for example flow cytometry. However, this traditional labelling-based detection requires complicated cell staining and consumes long operation time. In addition, the high cost and limitation of antibodies prevent this method from developing toward wide applications. Nowadays, biosensors based on metamaterials to detect biological substances have attracted great attention due to a lot of advantages, such as less cost, being time-saving and real-time detection of biomolecular interactions.[1–6] Moreover, such biosensors can simultaneously probe structural and binding characteristics of biomolecular interactions,[7] exhibiting a desirable performance in biological applications.[8–15] However, there are also inevitable shortcomings in metamaterial biosensors. Their low sensitivity and the lack of biological information also limit the development of these biosensors toward high performance. For this reason, a specifically designed metamaterial biosensor based on higher order Fano resonances is suggested.[16,17]

The improved sensitivity of biosensors based on higher order Fano resonant metamaterials (FRMMs) is caused by the sharp optical responses and strong local field. The surface plasmon characteristics of higher order Fano resonances supply a powerful photonic platform for metamaterial biosensors.[7,17–21] In general, a Fano resonance would occur when a broad excitation mode (bright mode) interferes with a narrow excitation mode (dark mode) in a frequency range as a result of the asymmetric designs of metamaterials.[5,16,21,22] The dipolar (D) plasmon resonance with high radiative loss usually serves as the bright mode, which can be directly excited by normally incident light. Instead, the higher order resonances such as quadrupolar (Q), octupolar (O), hexadecapolar (H), and triakontadipolar (T) plasmon resonances serve as the dark mode.[23–29] The coupling between the two modes brings the

[a]School of Opto-Electronic Engineering, Zaozhuang University, Zaozhuang, China. E-mail: 2111803010@stmail.ujs.edu.cn
[b]College of Precision Instrument and Opto-electronics Engineering, Tianjin University, Tianjin, China
[c]School of Mechanical Engineering Jiangsu University, Zhenjiang, China
[d]Advantest (China) Co., Ltd, Shanghai, China
[e]Department of Medical Oncology, Zaozhuang Municipal Hospital, Zaozhuang, China

†Electronic supplementary information (ESI) available. See DOI: 10.1039/c9nr07777d

‡These authors contributed equally to this work.

typically asymmetric Fano lineshape in the frequency spectrum with sharper peaks.[30–32] Such a high *Q*-factor property provides significant advantages in the application of biological and chemical sensors.[13] Furthermore, under the influence of the external environment, the frequency shift increases with the improving order of the resonance mode.

In this paper, we designed a split ring resonator composed of an asymmetric U-shaped resonator and a rectangle bar resonator to generate higher order Fano resonances. The quadrupolar (Q_x), octupolar (O_x), and hexadecapolar (H_x) Fano resonances excited by *x*-polarized THz waves and quadrupolar (Q_y) and octupolar (O_y) Fano resonances excited by *y*-polarized THz waves are observed at the frequencies of 1.19, 2.89, 3.93, 1.25 and 2.33 THz, respectively. In experiments, lung cancer cells with different concentrations can be intuitively detected by the shapes and distributions of graphics integrated with the frequency shift (Δf) for each resonant mode. On the other hand, as far as we know, we firstly observe that with the increase of the cell concentration, the variation of frequency shifts Δf at the Q_x, Q_y and O_y Fano resonances undergoes an increasing frequency shift stage (IFSS), decreasing frequency shift stage (DFSS), and re-increasing frequency shift stage (RIFSS). To further discuss the underlying physical mechanism, the generation of the DFSS is discussed by employing the amended perturbation theory. By employing this theory to fit the simulation results, the theoretical curves agree well with the simulated ones. Such a multiple mode integrated biosensor based on higher order FRMMs becomes especially attractive because it can offer opportunities for obtaining dielectric information of analytes, which is of great potential in label-free biosensing in future biomedical and biological applications.

Results and discussion

The schematic diagram of the unit cell for the proposed higher order FRMMs is displayed in Fig. 1(a). The structure is composed of two plasmonic components: a bar resonator acting as an electric dipole antenna and an asymmetric U-shaped resonator serving as a higher order mode antenna. In simulation, the two resonators are placed on a polyimide substrate whose permittivity ε and tan δ are measured to be 3.1 and 0.05, respectively. The numerical simulations are carried out by employing the finite difference time domain method implemented in the commercial software CST Microwave Studio. The simulated *x*-polarized and *y*-polarized transmittance spectra are shown in Fig. 1(b). In experiments, the THz waves along the *z* axis normally illuminate the samples. The schematic diagram for the periodic structure is shown in Fig. 1(c). The *x*-polarized and *y*-polarized transmittance spectra are measured by using a THz-TDS system (ADVANTEST TAS7500SU) and plotted in Fig. 1(d). Compared with Fig. 1(b), it is found that the transmittance curves under the incident of two polarized THz waves in experiments acquire a relatively good agreement with those of the simulations except for some discrepancy in the transmission amplitude and resonant peak

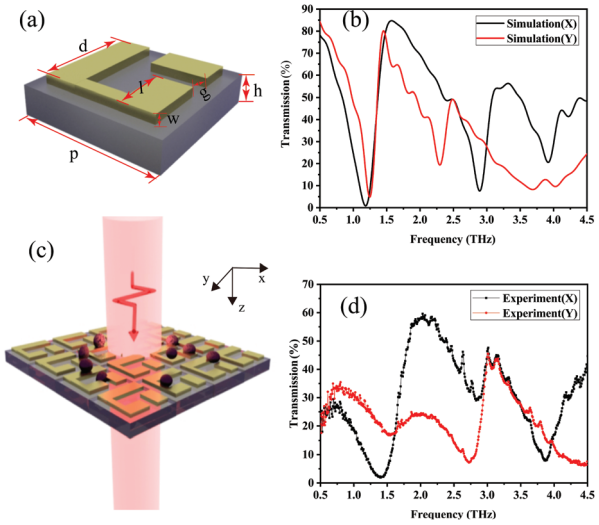

Fig. 1 (a) Schematic diagram of the unit cells for the high order FRMMs; the corresponding structural parameters are p = 50 μm, w = 200 nm, l = 20 μm, d = 40 μm, g = 8 μm, and h = 10 μm. (b) Simulated transmittance spectra for the *x*-polarized (black curve) and the *y*-polarized (red curve) incidence waves. (c) Schematic diagram for the periodic structure. (d) Experimental transmittance spectra for the *x*-polarized (black dotted curve) and the y-polarized (red dotted curve) incidence wave.

position, which can be attributed to the fabrication deviation of unit cells and the larger dielectric loss of practical materials.

To analyze the physical mechanism of the higher order Fano resonances under the excitation of *x*-polarized and *y*-polarized THz waves, the electric field distribution of the FRMMs is shown in Fig. 2. The two arms of the U-shaped resonator break the spatial symmetry of the structure due to the different length, which determines the degree of asymmetry. Such spatial symmetry breaking induces the coupling of the electric dipole mode and higher order modes. The transmittance curve of *x*-polarized THz waves and the electric field distribution of the *z*-component for higher order Fano resonances are shown in Fig. 2(a) and (b), respectively. The asymmetric configuration generates 4, 6 and 8 nodes in the electric field distribution of the FRMMs, which are denoted as Q_x, O_x and H_x modes, respectively.[16,17] On the other hand, the transmittance curve of *y*-polarized THz waves and the near field distribution of the *z*-component for higher order Fano resonances are shown in Fig. 2(c) and (d), respectively. The 4 and 6 nodes in the electric field distribution of the FRMMs demonstrate another two higher order Fano resonant modes, which are denoted as Q_y and O_y, respectively.

In order to explore the sensitive properties of higher order modes of FRMMs, lung cancer cells are adopted as analytes. The process of cell culturing is schematically shown in Fig. 3. The presence of cancer cells with certain concentrations changes the dielectric environment of the higher order FRMMs and leads to frequency shifts.[7] Before the experiment, we use an analyte layer with a thickness of 11 μm to simulate

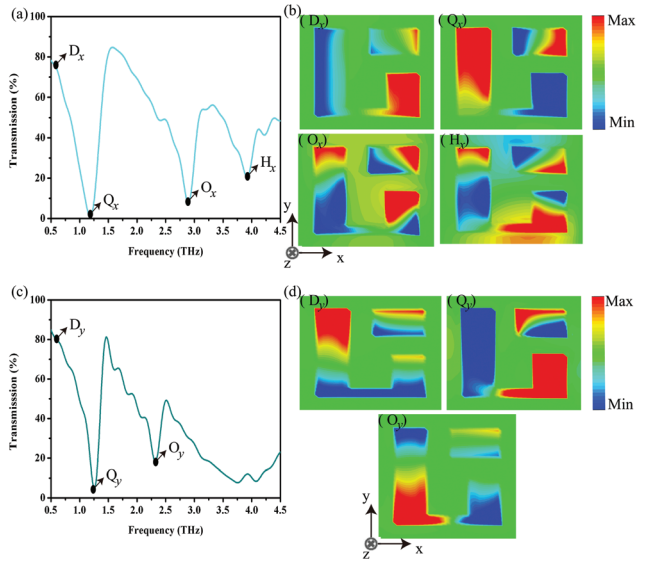

Fig. 2 (a) The simulated transmittance spectra for the *x*-polarized incidence wave. (b) The electric field distribution of the D_x (dipole), Q_x (quadrupolar), O_x (octupolar) and H_x (hexadecapolar) Fano resonances for the *x*-polarized wave. (c) The simulated transmittance spectra for the *y*-polarized incidence wave. (d) The electric field distribution of the D_y (dipole), Q_y (quadrupolar), and O_y (octupolar) Fano resonances for the *y*-polarized wave.

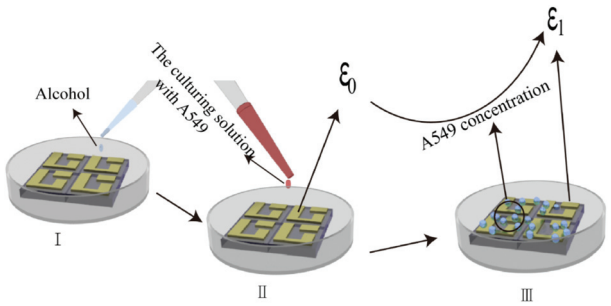

Fig. 3 Schematic representation of the cell culturing method on higher order FRMM-based biosensors with A549 cells binding to the metal surface and its equivalent dielectric environment transition mechanism.

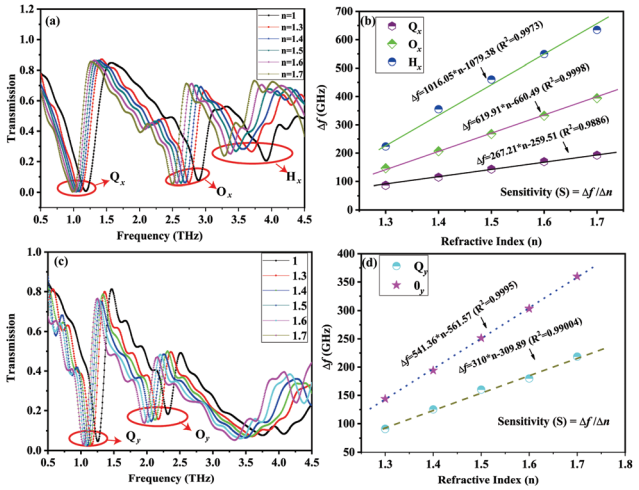

Fig. 4 Simulation transmission curve and frequency shift. (a) The *x*-polarized transmission curve with the analyte refractive index increasing from 1 to 1.7. (b) The *x*-polarized frequency shift under the different refractive indices of the analyte extracted from (a). (c) The *y*-polarized transmission curve with the analyte refractive index increasing from 1 to 1.7. (d) The *y*-polarized frequency shift under the different refractive indices of the analyte extracted from (c).

the dielectric environment which is described by the dielectric constant ε of the analyte layer. In order to study the biosensing performance of the proposed higher order FRMMs, firstly we calculate the theoretical sensitivity defined by the derivative of the resonance frequency shift to the change of refractive index. Fig. 4(a) shows that with the refractive index n varying from 1 to 1.7, the Q_x-dip, O_x-dip and H_x-dip show obvious red-shifts, which change from 1.21 to 0.9 THz, 2.88 to 2.4 THz and 3.8 to 3.3 THz, respectively. Moreover, the dependence of the relative frequency shifts $\Delta f = f^{(n)} - f^{(\mathrm{bare})}$ on the refractive index of the analyte layer is extracted and shown in Fig. 4(b). Obviously, the curves exhibit a linear relationship between Δf and n. Thus, the sensitivity S can be acquired by calculating the corresponding derivative of the Δf–n curve. The theoretical sensitivity S for different higher order modes (Q_x-dip, O_x-dip and H_x-dip) is calculated to be up to 267.12, 619.91 and 1016.5 GHz RIU^{-1} (RIU, Refractive Index Unit) respectively. These results are mostly superior to those of previous studies, which induces the conclusion that the same refractive index variation could cause larger frequency shifts with mode order increases.[12,15,17] In addition, the simulated *y*-polarized transmittance spectrum of the proposed higher order FRMMs with an analyte layer (n = 1, 1.3, 1.4, 1.5, 1.6 and 1.7) is displayed in Fig. 4(c). Similarly, with the change of refractive index, the Q_y-dip and O_y-dip red-shift from 1.3 to 1.1 THz and 2.3 to 1.9 THz respectively. The effect of refractive index of the analyte layer on the Δf also presents a linear relationship, as shown in Fig. 4(d). The resultant sensitivity of the Q_y-dip (~310 GHz RIU^{-1}) is larger than that of the *x*-polarized Q_x-dip with 267.21 GHz RIU^{-1}. Yet, the sensitivity of the O_y-dip (~541.36 GHz RIU^{-1}) is smaller than that of the *x*-polarized O_x-dip with 619.91 GHz RIU^{-1}. These results suggest that the property of the FRMM biosensor platform displays abundant sensing information from multiple resonant higher modes for biosensor platforms.

Owing to their high theoretical sensitivity and multidimensional information provision, it is greatly promising to employ the higher order FRMMs as a biosensor platform. Here, we cultured six concentrations (at the levels of 1×10^4, 3×10^4, 5×10^4, 1×10^5, 3×10^5 and 5×10^5 cells per ml) of lung cancer cells A549 on the surface of the higher order FRMMs to verify their sensing performance. The lung cancer cell line A549 was obtained from the Cell Bank of the Chinese Academy of Sciences (Shanghai, China). Fig. 5 shows the micrographs of the higher order FRMM-based biosensors with a cancer cell concentration increasing from 1×10^4 to 5×10^5 cells per ml. It can be seen that the number of adherent cells on the surface of the high order FRMMs sample increases gradually.

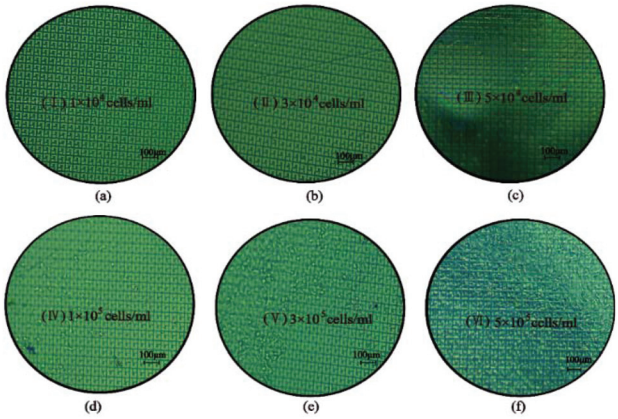

Fig. 5 Micrographs of the higher order FRMM-based biosensor with A549 cells at different concentrations changing from 1×10^4 cells per ml to 5×10^5 cell per ml.

Particularly, when the cell concentration reaches 5×10^5 cells per ml, the surface of the higher order FRMM sample is almost covered by cells. Considering the fabrication errors of samples, the resonant frequency of each sample may not appear at the same positions. If we only select one sample to be a bare comparison in all experiments, the accurate frequency shift is hard to determine. In order to solve such a problem, the transmittance spectrum of every higher order FRMM sample is measured in advance before culturing the corresponding cell concentration on it. Under these conditions, the resonant frequency is represented as $f_i^{(\mathrm{bare})}$ (i = 1, 2, 3, 4, 5, and 6). When the cell culturing is finished, we again measure the transmittance spectrum of every sample with cells adhered on it and take its resonant frequency to be $f_i^{(\mathrm{cells})}$ (i = 1, 2, 3, 4, 5, and 6). Thus, the relative frequency shift is defined as $\Delta f = f_i^{(\mathrm{cells})} - f_i^{(\mathrm{bare})}$. Fig. 6a–f show the measured x-polarized transmittance spectra of the higher order FRMMs at six cell concentrations, respectively. To improve the reliability of measurement, three repeated experimental tests for each cell concentration are performed and the corresponding curves are plotted in the graphs. Also, the relative frequency shift Δf of the Q_x-dip, O_x-dip and H_x-dip is extracted and displayed in Fig. 6h–j, respectively. For the Q_x-dip position, it can be observed from Fig. 6h that when the cell concentration is 1×10^4 cells per ml, the resonant frequency shows almost no shift, whereas after the cell concentration increases to 5×10^4 cells per ml, the Δf gradually increases. Interestingly, when the cell concentration approaches 1×10^5 cells per ml, the Δf drastically decreases, following that the Δf increases again with the growing cell concentration. Simultaneously, with the cell concentration increasing, the Δf at the O_x-dip and H_x-dip gradu-

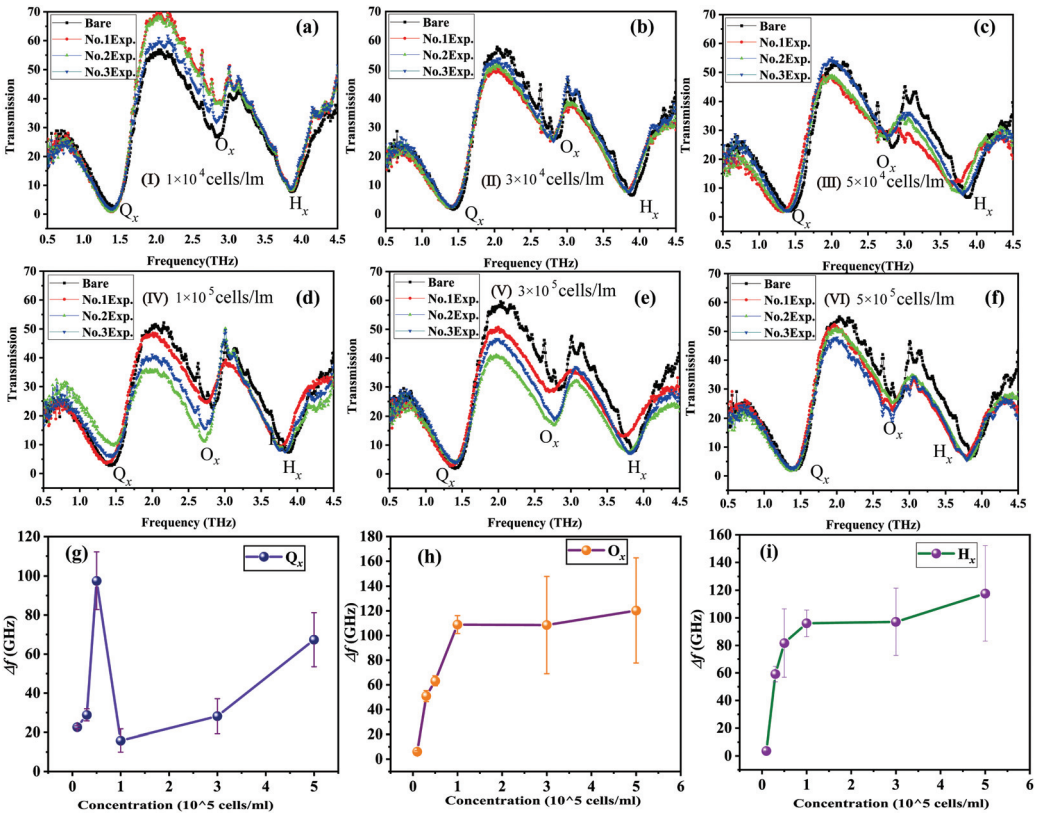

Fig. 6 The measured x-polarized transmittance spectrum of the proposed higher order FRMM-based biosensors under different cell concentrations (1×10^4 cells per ml, 3×10^4 cells per ml, 5×10^4 cells per ml, 1×10^5 cells per ml, 3×10^5 cells per ml, and 5×10^5 cells per ml). (h), (j), and (i) The measured x-polarized frequency shift Δf of Q_x, O_x and H_x extracted from (a), (b), (c), (d), (e), and (f).

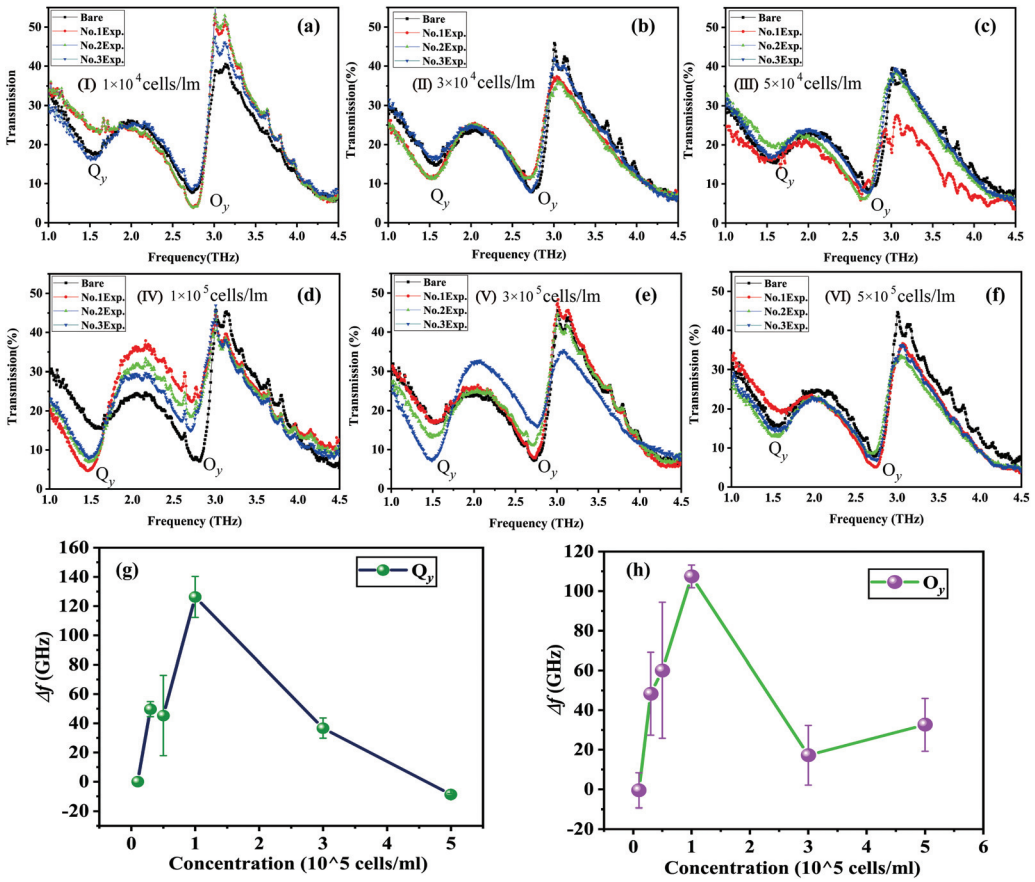

Fig. 7 The measured *y*-polarized transmittance spectrum of the designed higher order FRMM-based biosensors under different cell concentrations (1 × 10^4 cells per ml, 3 × 10^4 cells per ml, 5 × 10^4 cells per ml, 1 × 10^5 cells per ml, 3 × 10^5 cells per ml, and 5 × 10^5 cells per ml) (h) and (i) The measured *x*-polarized frequency shift Δf of Q_y and O_y extracted from (a), (b), (c), (d), (e), and (f).

ally increases. However, after the cell concentration increases to 1 × 10^5 cells per ml, the Δf at the O_x-dip and H_x-dip eventually tends to be constant. Additionally, the measured *y*-polarized transmittance spectra of the higher order FRMMs are shown in Fig. 7a–f, and the Δf of the Q_y-dip and O_y-dip is extracted and displayed in Fig. 7h and i, respectively. The observation from Fig. 7h shows that the Δf of the Q_y-dip increases with the increase of the cell concentration from 0.1 × 10^4 to 1 × 10^5 cells per ml. Instead, when the cell concentration changes from 1 × 10^5 to 5 × 10^5 cells per ml the Δf of the Q_y-dip falls off markedly. Moreover, the Δf of the O_y-dip has experienced a more complex change, and it can be seen from Fig. 7i that firstly the Δf of the O_y-dip has experienced an increasing process. When the cell concentration approaches 3 × 10^5 cells per ml, the Δf of O_y-dip experiences a drastically decreasing process. Finally, the Δf of the O_y-dip increases again with the growing cell concentration.

According to the above-mentioned analysis, each Fano resonance mold has its unique sensing characteristics under the influence of the dielectric environment. Such a unique sensing property makes the application of the multiple mode integrated biosensor possible. Furthermore, the integration of sensing performance for different order Fano resonance modes is more effective and accurate in detecting biological information. Fig. 8 shows the shapes and distributions of graphics integrated with the Δf for each resonance mode under different cell concentrations. It can observed that the different cell concentration can be intuitively detected by the shapes and distributions of graphics integrated with the frequency shift (Δf) for each reso-

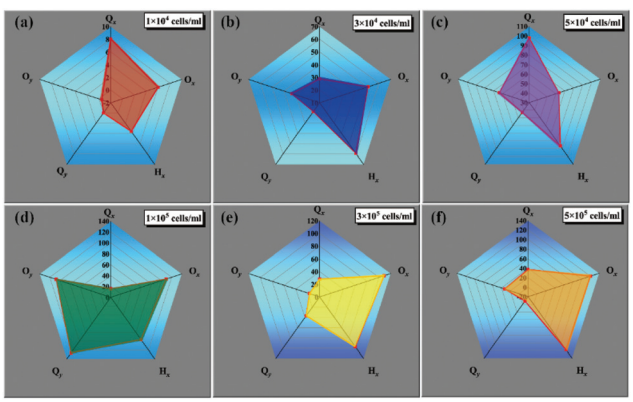

Fig. 8 The shapes and distributions of graphics integrated with the Δf for each resonant mode under different cell concentrations.

nance mode. For example, from Fig. 8a, when the cell concentration is 1×10^4 cells per ml, the shape of a pentagon formed by the Δf in different resonance modes is different from that of any other cell concentration. In addition, the distribution of the pentagon (red region) is mainly concentrated in the area enclosed by the center, Q_x, O_x and H_x, which is also different from that of any other cell concentration. Therefore, the multiple mode integrated biosensor shows excellent performance in specifically detecting biological information.

On the other hand, as shown in Fig. 6h, with the increase of the cell concentration, the Δf of the Q_x-dip has experienced three different stages which are defined as an increasing frequency shift stage (IFSS), decreasing frequency shift stage (DFSS), and re-increasing frequency shift stage (RIFSS). The observation of the DFSS is indeed abnormal, because as far as we know, metamaterial-based biosensors only exhibit the IFSS with the change of analyte characteristics such as refractive index, thickness and concentration in various present studies.[2,33,34] The extraordinary DFSS implies an anomalous response in the frequency shift. As to the O_x-dip and H_x-dip (Fig. 6i and j), however, such an unusual DFSS is not observed. Similarly, from Fig. 7h and i, it can be seen that the Δf of the Q_y-dip and O_y-dip also exhibits an obvious DFSS respectively. To verify the validity of the DFSS by judging the variation of Δf, single-factor analysis of variance (ANOVA) is used to evaluate the significant difference of the Δf at six cell concentrations. The difference degree of averaged Δf is considered statistically significant when $P < 0.05$. The different (or identical) letters ('a'–'g') in superscript in ESI Table 1† represent a significant (or insignificant) difference between every two experimental cases. For convenient comparison, the details of Δf values are given as well. It can be implied that the Δf is significantly influenced by cell concentrations. The unique superscript letter 'c' of Q_x (ESI Table S1†) for a cell concentration of 5×10^4 cells per ml implies a significant change ($P < 0.05$), which confirms the validity of the DFSS. However, there is no significant difference ($P > 0.05$) observed between 1×10^4 and 1×10^5, as well as 3×10^5 and 5×10^5 cells per ml. Furthermore, the O_x-dip is also significantly influenced by the cell concentration ($P < 0.05$) before the cell concentration reaches 1×10^5 cells per ml. After that, the difference turns out not to be significant ($P > 0.05$). In fact, this observation illustrates that when the cell concentration changes from 1×10^4 to 1×10^5 cells per ml, the more cells are growing on the higher order FRMM sample, the larger difference of Δf is. This result is in agreement with that of Yan *et al.* who reported that the Δf increases as the cell concentration is increased.[1] In addition, this also indicates that when the cell concentration increases to 1×10^5 cells per ml, the Δf may reach the detecting saturation of the higher order FRMM biosensor. The averaged Δf for the H_x-dip exhibits the same trend as that of the O_x-dip, as seen in ESI Table S1.† Similar to ESI Tables S1, ESI Table S2† shows that the averaged Δf based on the *y*-polarized higher order resonance is significantly influenced by both the cell concentration and the higher order mode of Fano resonances. The Δf of Q_y for a cell concentration of 1×10^5 cells per ml was significantly ($P < 0.05$) higher than that for other cell concentrations. This observation further demonstrates the evidence of the DFSS. The underlying physical mechanism of the anomalous DFSS can be interpreted by the effect of dielectric hemispheric balls with different refractive indices on the Δf in the simulations. The corresponding relationship for the Q_x-dip, O_x-dip and H_x-dip is given in Fig. 9a–c, respectively. From Fig. 9a and b, it can be seen that with the number of the dielectric balls increasing from 1 to 11 balls on the FRMMs, the Δf at the Q_x-dip and O_x-dip both experience the DFSS when the number of hemispheric balls approaches 9 under different refractive indexes, whereas after the frequency reaches a higher order mode at the H_x-dip, it can be found from Fig. 9c that the DFSS disappears no matter what the number of hemispheric balls and the refractive index are. Here, in order to explain the physical mechanism of the DFSS, we amend perturbation theory by introducing a new dielectric constant ε_f. However, commonly, the relationship between the change of the dielectric environment and the Δf can be described by perturbation theory. The relative change of angular frequency $\Delta\omega/\omega_0$ can be calculated by the following equation:[7,15]

$$\frac{\Delta\omega_m}{\omega_m} = -\frac{1}{2}\frac{\int_0^{h_{cell}} E_m(r)\cdot(\varepsilon-1)\cdot E_m(r)\mathrm{d}r}{\int_0^{\infty}|E_m|^2\cdot \mathrm{d}r} \quad (1)$$

where $E_m(r)$ is the electric field and ε is the equivalent dielectric constant of the higher order FRMMs. Because the electric field decays exponentially along the direction normal to the metamaterial, the frequency shift calculated from eqn (1) scales with the analytes as follows:[15]

$$\frac{\Delta\omega_m}{\omega_m} \propto \frac{(\varepsilon-1)h_{cell}}{l_{field}} \quad (2)$$

$$\varepsilon_{cell} = \varepsilon - 1 \quad (3)$$

where ε_{cell} is the difference of the equivalent dielectric constant between the bare and analytes (cancer cells); h_{cell} is the equivalent thickness of the analyte layer; and l_{field} is the penetration depth of the THz field. According to eqn (2) and (3), the equivalent dielectric constant of single-layer cells (ε_{cell}) is proportional to the cell number, and because $h_{cell} > 0$, $l_{field} > 0$, indicating that the increase of the cell concentration will cause an increase of the resonant frequency shift.[15] That is to say, as the cell concentration increases, the Δf of the Q_x-dip, Q_y-dip and O_y-dip must increase and there is an increase function relationship between the Δf and the cell concentration. In this case, the DFSS is unlikely to appear. Such a conclusion is contradictory to the observations in previous simulation and experimental results, in which the DFSS is displayed in the Δf-related curves. Therefore, we guessed that a special electromagnetic response has occurred in the multipolar Fano resonance system. In addition, some previous studies reported that the negative resonance response has occurred in the multipolar Fano resonance system. For example, Chen *et al.* observed a net negative optical scattering force based on Ag core–shell

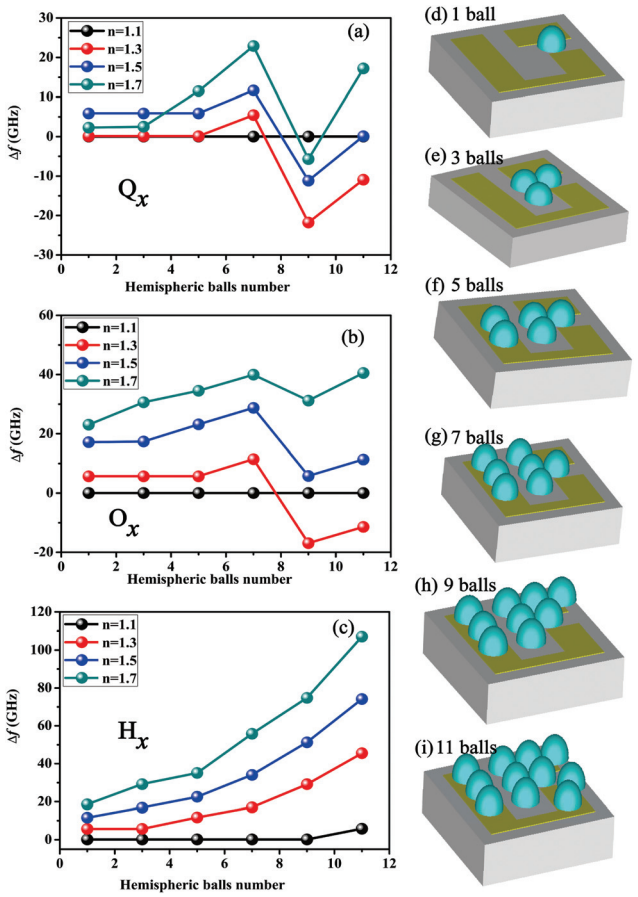

Fig. 9 The simulated x-polarized frequency shift Δf under different number dielectric hemispheric balls with a refractive index from 1 to 1.7. (a) Q_x-dip, (b) O_x-dip, and (c) H_x-dip.

particles.[35] And it has been proved that the negative resonance response in the material leads to a negative value of equivalent permittivity.[36,37] Therefore, we guessed that our designed multipolar Fano resonance system may produce a negative equivalent permittivity under some specific conditions. Based on the above analysis, we amend perturbation theory to explain the occurrence of the DFSS as follows:

$$\varepsilon_{\text{cell}} = (\varepsilon + \varepsilon_{\text{f}}) - 1 \tag{4}$$

where w is a coefficient and ε_{f} is the amending dielectric constant.

In order to test whether this amended perturbation theory is suitable for describing the variation of Δf in the DFSS, the Δf values of Q_x, O_x and H_x are taken as examples for statistical analysis. In this analysis, the refractive index is adopted changing from 1.1 to 2.3 and 9 balls are fixed at the appropriate position. Non-linear regression analysis is applied to calculate the fitting parameters of the amended perturbation theory. The coefficient of correlation (R^2) is used as the primary criterion to examine the amended perturbation theory. A higher R value is considered as the criterion for goodness of fit and the highest value is 1.[38,39] In other words, the value of R^2 is higher, the amended perturbation theory is more suitable for describing the variation of Δf in the DFSS range. It can be calculated as follows:[39]

$$R^2 = \frac{\sum_{i=1}^{N}(\Delta f_i - \Delta f_{\text{pre},i}) \cdot \sum_{i=1}^{N}(\Delta f_i - \Delta f_{\text{sim},i})}{\sqrt{\left[\sum_{i=1}^{N}(\Delta f_i - \Delta f_{\text{pre},i})^2\right] \cdot \left[\sum_{i=1}^{N}(\Delta f_i - \Delta f_{\text{sim},i})^2\right]}} \tag{5}$$

where $\Delta f_{\text{sim},i}$ is the ith simulation frequency shift, $\Delta f_{\text{pre},i}$ is the ith predicted frequency shift, N is the number of simulation,

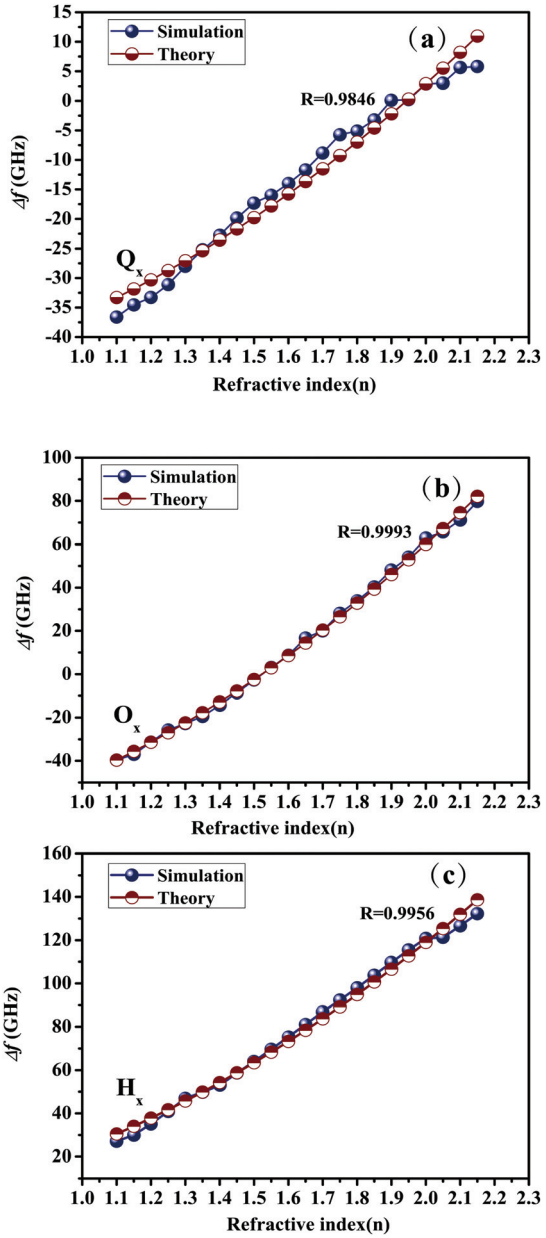

Fig. 10 The comparison between the simulated x-polarized frequency shift Δf and theoretical calculations when the number of dielectric hemispheric balls with a refractive index from 1.1 to 2.3 is fixed at 9. (a) Q_x-dip, (b) O_x-dip, and (c) H_x-dip.

and n is the number of constants in the amended perturbation theory. By using eqn (4), simulation frequency shifts Δf of Q_x, O_x and H_x are theoretically fitted based on amended perturbation theory, as depicted in Fig. 10. It can be observed from Fig. 10a–c that the theoretical fitting curves (Δf *versus* refractive index) show a relatively good agreement with the simulation. In addition, the values of R^2 for Q_x, O_x and H_x in the amended perturbation theory change from 0.9846 to 0.9993 respectively (Fig. 10). These values are greater than 0.97, indicating a good fit.[38] Therefore, the amended perturbation theory is considered as a suitable model to describe the variation of Δf in the DFSS. ESI Table S3† shows the values of coefficients of w changing from 38.90 to 107.05 and ε_f from −2.77751 to 0.7508 fitted by the amended perturbation theory, respectively. In simulation, the w is a proportional coefficient of the amended perturbation theory, and the fixed values of h_{cell} (m) and l_{field} are given as 5.00×10^{-6} and 1.50×10^{-5} m, respectively. From the amended perturbation theory, with increasing mode order from Q_x to O_x, the ε_f parameters change from −2.7775 to −1.3195 respectively. Therefore, the anomalous DFSS appears due to the negative ε_f. On the other hand, the ε_f parameter for H_x is 0.7508, which implies that the DFSS disappears with the increase of cell concentration. The fitting results theoretically confirm that the negative ε_f parameter would lead to the DFSS in the resonant frequency shift of higher order Fano resonances.

Conclusions

In summary, higher order FRMM samples have been fabricated and employed to detect different A549 concentrations. The lung cancer cells with different concentrations can be intuitively detected by the shapes and distributions of graphics integrated with the frequency shift (Δf) for each resonant mode. Furthermore, an anomalous response in the frequency shift Δf in resonant modes is surprisingly observed. The originally amended perturbation theory is proposed to explain the anomalous response. The fitting results suggest that the amended perturbation theory model is considered as a suitable model to describe the DFSS. The proposed multiple mode integrated biosensor based on higher order FRMMs may offer a highly sensitive, specific platform for fast and low-cost cell detection from the physical perspective.

Conflicts of interest

There are no conflicts to declare.

Acknowledgements

This work was supported by the National Natural Science Foundation of China (NSFC) (61701434, 61735010, and 61675147); the China Postdoctoral Science Foundation (2015M571263); the Natural Science Foundation of Shandong Province (ZR2017MF005 and ZR2018LF001); the National Key Research and Development Program of China (2017YFA0700202 and 2017YFB1401203); the Shandong Province Higher Education Science and Technology Program (J17KA087); the Programe of Independent and Achievement Transformation plan for Zao Zhuang (2016GH19 and 2016GH31); the Project Special Funding of Taishan Schola; the funding by Qingchuang Science and Technology Plan of Shandong Universities (2019KJN001); the Zao zhuang Engineering Research Center of Terahertz; the Natural Science Foundation of Jiangsu Province (BK20180862); and the China Postdoctoral Fund (2019M651725) Jiangsu Provincial Graduate Research and Practice Innovation Project (KYCX19_1583).

References

1 X. Yan, M. Yang, Z. Zhang, L. Liang, D. Wei, M. Wang, M. Zhang, T. Wang, L. Liu, J. Xie and J. Yao, *Biosens. Bioelectron.*, 2019, **126**, 485–492.
2 Z. Zhang, H. Ding, X. Yan, L. Liang, D. Wei, M. Wang, Q. Yang and J. Yao, *Opt. Mater. Express*, 2018, **8**, 659.
3 A. Salim and S. Lim, *Biosens. Bioelectron.*, 2018, **117**, 398–402.
4 X. Wu, B. Quan, X. Pan, X. Xu, X. Lu, C. Gu and L. Wang, *Biosens. Bioelectron.*, 2013, **42**, 626–631.
5 S. H. Wu, K. L. Lee, A. Chiou, X. Cheng and P. K. Wei, *Small*, 2013, **9**, 3532–3540.
6 C. Cao, J. Zhang, X. Wen, S. L. Dodson, N. T. Dao, L. M. Wong, S. Wang, S. Li, A. T. Phan and Q. Xiong, *ACS Nano*, 2013, **7**, 7583–7591.
7 C. Wu, A. B. Khanikaev, R. Adato, N. Arju, A. A. Yanik, H. Altug and G. Shvets, *Nat. Mater.*, 2011, **11**, 69–75.
8 L.-H. Du, J. Li, Q. Liu, J.-H. Zhao and L.-G. Zhu, *Opt. Mater. Express*, 2017, **7**, 1335.
9 H.-J. Lee, J.-H. Lee and H.-I. Jung, *Appl. Phys. Lett.*, 2011, **99**, 163703.
10 A. A. Yanik, A. E. Cetin, M. Huang, A. Artar, S. H. Mousavi, A. Khanikaev, J. H. Connor, G. Shvets and H. Altug, *Proc. Natl. Acad. Sci. U. S. A.*, 2011, **108**, 11784–11789.
11 S. Zhang, K. Bao, N. J. Halas, H. Xu and P. Nordlander, *Nano Lett.*, 2011, **11**, 1657–1663.
12 T. Beni, N. Yamasaku, T. Kurotsu, N. To, S. Okazaki, T. Arakawa, A. Balcytis, G. Seniutinas, S. Juodkazis and Y. Nishijima, *ACS Sens.*, 2019, **4**(9), 2389–2394.
13 R. Singh, W. Cao, I. Al-Naib, L. Cong, W. Withayachumnankul and W. Zhang, *Appl. Phys. Lett.*, 2014, **105**, 171101.
14 Y. Yang, I.I Kravchenko, D. P. Briggs and J. Valentine, *Nat. Commun.*, 2014, **5**, 5753.
15 C. Zhang, L. Liang, L. Ding, B. Jin, Y. Hou, C. Li, L. Jiang, W. Liu, W. Hu, Y. Lu, L. Kang, W. Xu, J. Chen and P. Wu, *Appl. Phys. Lett.*, 2016, **108**, 241105.
16 Y. H. Fu, J. B. Zhang, Y. F. Yu and B. Luk'yanchuk, *ACS Nano*, 2012, **6**, 5130–5137.
17 X. Guo, H. Hu, X. Zhu, X. Yang and Q. Dai, *Nanoscale*, 2017, **9**, 14998–15004.

18 F. B. Zarrabi, M. Bazgir, S. Ebrahimi and A. Saee Arezoomand, *J. Electromagn. Waves Appl.*, 2017, **31**, 1444–1452.
19 Z. Li, S. Cakmakyapan, B. Butun, C. Daskalaki, S. Tzortzakis, X. Yang and E. Ozbay, *Opt. Express*, 2014, **22**, 26572–26584.
20 B. Luk'yanchuk, N. I. Zheludev, S. A. Maier, N. J. Halas, P. Nordlander, H. Giessen and C. T. Chong, *Nat. Mater.*, 2010, **9**, 707–715.
21 R. S. John, F. O'Hara, I. Brener, E. Smirnova, J. Han, A. J. Taylor and W. Zhang, *Opt. Express*, 2008, **16**, 1786.
22 Y. K. Srivastava, L. Cong and R. Singh, *Appl. Phys. Lett.*, 2017, **111**, 201101.
23 W. X. Lim and R. Singh, *Nano Convergence*, 2018, **5**, 5.
24 M. Manjappa, P. Pitchappa, N. Singh, N. Wang, N. I. Zheludev, C. Lee and R. Singh, *Nat. Commun.*, 2018, **9**, 4056.
25 Y. K. Srivastava, R. T. Ako, M. Gupta, M. Bhaskaran, S. Sriram and R. Singh, *Appl. Phys. Lett.*, 2019, **115**, 151105.
26 Y. Bao, Z. Hu, Z. Li, X. Zhu and Z. Fang, *Small*, 2015, **11**, 2177–2181.
27 N. Dabidian, I. Kholmanov, A. B. Khanikaev, K. Tatar, S. Trendafilov, S. H. Mousavi, C. Magnuson, R. S. Ruoff and G. Shvets, *ACS Photonics*, 2015, **2**, 216–227.
28 Y. Moritake, Y. Kanamori and K. Hane, *Opt. Express*, 2016, **24**, 9332–9339.
29 M. H. Daniel Dregely and H. Giessen, *ACS Nano*, 2011, **5**(10), 8202–8211.
30 Y. K. Srivastava, M. Manjappa, L. Cong, W. Cao, I. Al-Naib, W. Zhang and R. Singh, *Adv. Opt. Mater.*, 2016, **4**, 457–463.
31 C. Ding, L. Wu, D. Xu, J. Yao and X. Sun, *Opt. Commun.*, 2016, **370**, 116–121.
32 I. Al-Naib, *J. Infrared, Millimeter, Terahertz Waves*, 2017, **39**, 1–5.
33 M. Yang, L. Liang, Z. Zhang, Y. Xin, D. Wei, X. Song, H. Zhang, Y. Lu, M. Wang, M. Zhang, T. Wang and J. Yao, *Opt. Express*, 2019, **27**, 19520.
34 B. Reinhard, K. M. Schmitt, V. Wollrab, J. Neu, R. Beigang and M. Rahm, *Appl. Phys. Lett.*, 2012, **100**, 221101.
35 S. L. Huajin Chen, J. Zi and Z. Lin, *ACS Nano*, 2015, **9**(2), 1926–1935.
36 D. R. Smith, J. B. Pendry and M. C. Wiltshire, *Science*, 2004, **305**, 788–792.
37 J. Valentine, S. Zhang, T. Zentgraf, E. Ulin-Avila, D. A. Genov, G. Bartal and X. Zhang, *Nature*, 2008, **455**, 376–379.
38 S. Taghian Dinani, N. Hamdami, M. Shahedi and M. Havet, *Energy Convers. Manage.*, 2014, **86**, 70–80.
39 M. Yang and C. Ding, *SpringerPlus*, 2016, **5**, 909.